Hydrogenation of aqueous nitrate and nitrite with ruthenium catalysts

Xiangchen Huo,[1] Daniel J. Van Hoomissen,[2] Jinyong Liu,[1] Shubham Vyas,[2] Timothy J. Strathmann[1*]

[1]Department of Civil and Environmental Engineering and [2]Department of Chemistry and Geochemistry, Colorado School of Mines, Golden, Colorado 80401, United States

*Corresponding author: phone: +1-303-384-2226, E-mail: strthmnn@mines.edu

Abstract - Historically, development of catalysts for treatment of nitrate-contaminated water has focused on supported Pd-based catalysts, but high costs of the Pd present a barrier to commercialization. As part of an effort to develop lower cost hydrogenation catalysts for water treatment applications, we investigated catalysts incorporating Ru with lower cost. Pseudo-first-order rate constants and turnover frequencies were determined for carbon- and alumina-supported Ru and demonstrated Ru's high activity for hydrogenation of nitrate at ambient temperature and H_2 pressure. *Ex situ* gas pretreatment of the catalysts was found to enhance nitrate reduction activity by removing catalyst surface contaminants and exposing highly reducible surface Ru oxides. Ru reduces nitrate selectively to ammonium, and no aqueous nitrite intermediate is observed during reactions. In contrast, reactions initiated with nitrite yield a mixture of two endproducts, with selectivity shifting from ammonium towards N_2 at increasing initial aqueous nitrite concentrations. Experimental observation and Density Functional Theory calculations

together support a reaction mechanism wherein sequential hydrogenation of nitrate to nitrite and NO is followed by parallel pathways involving the adsorbed NO: (1) sequential hydrogenation to ammonium, and (2) N-N coupling with aqueous nitrite followed by hydrogenation to the detected N_2O intermediate and N_2 endproduct. These findings open the door to development of alternative catalysts for purifying and recovering nutrients from nitrate-contaminated water sources, and insights into the controlling surface reaction mechanisms can guide rational design efforts aimed at increasing activity and tuning endproduct selectivity.

Keywords: Ruthenium catalysts, nitrate reduction, catalyst pretreatment, isotope labeling, density functional theory

1. Introduction

Nitrate contamination of drinking water sources is among the greatest public health threats around the world [1]. Nitrate concentrations exceeding health-based standards are routinely detected in drinking water sources due to excess fertilizer applications and release of incompletely treated industrial and domestic wastewater [2-4]. The growing contamination of drinking water sources raises health concerns because nitrate can be transformed into hazardous chemicals, including nitrite, which causes methemoglobinemia (i.e., blue baby syndrome), and potentially carcinogenic nitrosamines [5, 6]. As a result, there is great interest in the development of efficient, robust and low-cost technologies for treating nitrate-contaminated water.

Several technologies are available to separate nitrate from water, including ion exchange [7, 8], high pressure membrane filtration [9], and electrodialysis [10], and have demonstrated their effectiveness in full-scale practice [2, 11]. The principal drawback of these systems is the production of a nitrate concentrate stream that requires further treatment before disposal [12, 13]. Biological denitrification is widely used for the treatment of municipal and industrial wastewater, but concerns about pathogen introduction, the need for costly organic carbon amendments and potential residuals, and biological sludge production have limited application for drinking water treatment [14, 15]. More recently, chemical reduction of nitrate has been increasingly explored. Zerovalent metals, including iron [16], aluminum [17], and magnesium [18], stoichiometrically couple nitrate reduction with metal corrosion,

but reactions are hindered by the formation of oxide surface coatings, and the need to constantly replenish the metals as reducing equivalents are consumed creates operational challenges.

As an alternative to stoichiometric metal reductants, our team and others have been investigating the application of metal hydrogenation catalysts that couple nitrate reduction with H_2 oxidation [7, 19-23]. Nitrate can be transformed into two endproducts with different H_2 and acidity requirements:

$$NO_3^- + 2.5H_2 + H^+ \xrightarrow{catalyst} 0.5N_2 + 3H_2O \quad (1)$$

$$NO_3^- + 4H_2 + 2H^+ \xrightarrow{catalyst} NH_4^+ + 3H_2O \quad (2)$$

Because the metals are acting as catalysts rather than stoichiometric reactants, they are not consumed in the process or generate a secondary solid waste stream that requires disposal. H_2 is an inexpensive electron donor that has lower life cycle environmental impacts than organic electron donors applied in most biological denitrification processes [24]. To date, most work has focused on the development of nitrate and nitrite treatment processes employing supported Pd-based catalysts [13, 25, 26]. Pd catalysts are highly effective in converting nitrite, the first daughter product of nitrate reduction, to harmless N_2 gas at an incomparable rate [27-29], but monometallic Pd catalysts show little reactivity with nitrate [30, 31]. Deposition of a second "promoter" metal (e.g., Cu, In, Sn) together with Pd is typically required to facilitate reduction of nitrate to nitrite [23, 31, 32]. A large body of literature has reported on aqueous nitrate reduction with Pd-based bimetallic catalysts [20, 30, 31, 33-37], and our current understanding of metal-catalyzed nitrate hydrogenation mechanisms has been limited to reactions occurring with these materials. The prevailing reaction pathway follows a two-step process depicted in Scheme 1: (1)

hydrogenation of nitrate to nitrite on bimetallic clusters followed by (2) further hydrogenation of nitrite on Pd sites to a mixture of N_2 and ammonium stable endproducts, the net processes being reflected by Eqs. (1-2) [22, 35, 38-40]. The proposed sequential reduction pathway is supported by the observation of nitrite as a transient reaction intermediate [23, 33], increasing with pH as the rate of Pd-catalyzed nitrite reduction decreases [39, 41], and isotope labeling experiments showing Pd-catalyzed reduction of NO to the same mixture of endproducts and selective conversion of N_2O to N_2 [22]. The distribution of endproducts, presumed to be controlled by the Pd-catalyzed reactions of nitrite or its daughter products (e.g., adsorbed NO), has been reported to vary with catalyst composition [31], metal nanoparticle size [42], support [43], and solution pH [44].

Although years of effort have been invested in improving the activity, endproduct selectivity, and long-term stability of Pd-based bimetallic catalysts [31, 45] (and to a lesser extent Pt-based catalysts [36, 46]), deployment of practical catalytic treatment systems remains limited, in large part, due to high costs of Pd [47]. Precious metal-free catalysts based on Ni have been explored [15, 48, 49], but instability in aqueous matrices [50], and serious concerns about the associated leaching of dissolved Ni^{2+} [51] and the pyrophoric nature of highly active Raney Ni [52] have limited further development efforts.

As a result of the low nitrate and nitrite reduction activity reported in early catalyst screening studies [27, 28], Ru hydrogenation catalysts have been largely overlooked for such applications. However, a renewed examination of the application of Ru-based catalysts is warranted because of the historically much lower price of Ru in comparison to Pd and Pt [47] as well as the metal's documented catalytic

activity for a diverse range of reactions, including hydrogenation, hydrodeoxygenation and hydrodechlorination reactions [53, 54]. In addition, work on electrochemical reduction of nitrate (in acidic media) has shown that Ru electrodes exhibit higher activity than Pt, Pd and Ir electrodes [55]. After recently screening a range of metal catalysts as alternatives to Pd for reduction of oxyanion pollutants [56], this contribution focuses on a renewed evaluation of the kinetics and mechanisms of nitrate and nitrite reduction by supported Ru catalysts. Reaction kinetics, product distribution analysis, and catalyst characterization studies are combined with Density Functional Theory (DFT) calculations to improve our understanding of interaction between nitrate (and nitrite) and Ru metal surfaces and elucidate the origin of endproduct selectivity.

2. Materials and methods

2.1. Catalysts

A full listing of chemical reagents is provided in Supporting Information (SI; Section S1). Ru and Pd catalysts immobilized on carbon and alumina supports (nominal 5 wt% metal) were purchased from Sigma-Aldrich. Unless otherwise noted, the as-received Ru and Pd catalysts were pretreated *ex situ* in flowing H_2 at 350°C for 2 h prior to use in aqueous oxyanion reduction experiments. The only exception to this was for experiments specifically examining the effects of different *ex situ* pretreatments (see section 3.2), wherein the as-received catalysts (no pretreatment), catalysts pretreated *ex situ* in flowing N_2 at 350°C for 2 h, and catalysts pretreated *ex situ* in flowing H_2 as mentioned above were compared.

No precautions were taken following pretreatment to avoid surface passivation upon exposure to air. Bimetallic Pd-Cu/C, Ru-Cu/C, and Ru-In/C catalysts were prepared by incipient wetness impregnation [57] of 1 wt% of Cu (as $Cu(NO_3)_2 \cdot 3H_2O$) or In (as $In(NO_3)_3 \cdot 3H_2O$) on as-received commercial Pd/C and Ru/C, respectively, followed by air drying at 110°C for 12 h and H_2 at 350 ℃ for 2 h.

Catalysts were extensively characterized, including metal content (inductively coupled plasma-optical emission spectrometry, ICP-OES), specific surface area and average pore diameter of the support materials (N_2 physisorption), metal dispersion (the percentage of Ru or Pd atoms present on the clean surface of the immobilized metal nanoparticles, CO chemisorption), active surface (the percentage of Ru or Pd atoms accessible to reactants under simulated *in situ* conditions, CO chemisorption), morphology and size of the metal nanoparticles (transmission electron microscopy and high-angle annular dark-field-scanning transmission electron microscopy, TEM and HAADF-STEM), Ru reducibility (H_2 temperature-programmed reduction, H_2 TPR), and long-range structural order (X-ray diffraction, XRD). Details of each methodology are provided in SI Section S2.

2.2. Nitrate and nitrite reduction kinetics

Aqueous nitrate and nitrite reduction kinetics were measured in an open semi-batch system under continuous H_2 sparging (1 atm, 40 $mL \cdot min^{-1}$) at constant temperature (25 ± 0.5 °C). A 250 mL three-neck reactor was filled with 150 mL deionized water and predetermined mass of catalyst. The suspension was sonicated for 5 min and sparged with H_2 gas for 30 min before introducing a small volume of $NaNO_3$ or $NaNO_2$ stock solution to initiate the reaction. Reaction progress was monitored by

periodic collection of suspension aliquots (1.5 mL) that were immediately filtered (0.22 μm cellulose acetate) to remove catalyst particles and quench reactions prior to analysis by ion chromatography (NO_3^- and NO_2^-) and colorimetric assay (NH_4^+). The suspension was mixed by a Teflon-coated magnetic stir bar at 700 rpm. Solution pH was maintained by HCl addition from an automatic pH-stat (Radiometer TitraLab 854). Catalyst activity was assessed by quantifying initial mass-normalized pseudo-first-order rate constants (k_0, $L \cdot g_{Ru/Pd}^{-1} \cdot min^{-1}$) and turnover frequencies (TOF_0, min^{-1}), defined as the number of nitrate or nitrite ions reduced per active surface site per minute. The active surface was estimated from CO chemisorption measurement using an assumed 1:1 CO:Metal adsorption stoichiometry [58, 59]. Additional details of the procedures for kinetics parameter calculations and aqueous analytical measurements are provided in SI Sections S3 and S4, respectively. A catalyst re-use experiment was carried out to evaluate the stability of Ru/C. After a semi-batch reaction was complete, the catalyst solid was collected on a filter (glass fiber filter; EMD Millipore), washed with deionized water several times, and vacuum dried at 65 ℃ overnight before re-suspending in water for the subsequent semi-batch reaction. The catalyst was also re-characterized after completion of the re-use experiment.

2.3. Isotope labeling experiments

Nitrogen mass balances and endproduct distributions were quantified using closed-bottle batch experiments with the aid of ^{15}N-labeled nitrate and nitrite salts to avoid the interference from atmospheric $^{14}N_2$ during mass spectrometry measurement of the N_2 endproduct [22]. A 160 mL serum bottle with 75 mL of an organic buffer, 4-morpholineethanesulfonic acid (MES) (pH 5.5, 40 mM), a

predetermined mass of catalyst, and a Teflon-coated magnetic stir bar was sealed by a 1.0 cm-thick rubber stopper held in place by an Al crimp cap. Experiments were conducted at ambient temperature (21 ± 1°C) and suspensions were mixed in the same manner as the semi-batch experiments. The reactor was sparged with H_2 for 30 min to saturate the headspace and solution before introducing the target oxyanion pollutant. A H_2-sparged stock solution of $Na^{15}NO_3$ or $Na^{15}NO_2$ was then added to the reactor to initiate the reaction, and 1.5 mL aqueous aliquots were withdrawn by syringe through the gas-tight septa to monitor disappearance of the parent reactant and the evolution of aqueous intermediates and products. Headspace samples (0.1 mL) were collected separately and immediately analyzed for labeled gaseous intermediates and products (^{15}NO, $^{15}N_2O$, and $^{15}N_2$) by gas chromatography-mass spectrometry (GC-MS, details in SI). Headspace gases were assumed to be maintained in equilibrium with the aqueous phase at all times [60], which was supported by good nitrogen mass balance closure. Analyte values in these experiments are reported in moles of nitrogen because products include both liquid and gas species as well as both mono- and diatomic nitrogen species. The total mass of H_2 initially added to the sealed batch reactor (~3.4 mmol) was in significant excess of the stoichiometric requirement for the complete reduction of the added NO_3^- to NH_4^+ (~0.5 mmol).

2.4. Computational methods

DFT calculations of N-containing species associated with Ru metal surfaces were performed with the Gaussian 09 suite of programs [61]. A Ru_{18} metal cluster structure was used to model Ru catalysts based on the work of Aguilera-Granja *et al*. [62] and Zhang *et al*. [63]. It was shown that Ru and Rh

clusters with fewer than 20 atoms adopt simple cubic or distorted cubic structure. Geometry optimizations of Ru clusters were completed at the PBE0 [64] level of theory with the Lanl2DZ basis set [65, 66]. The core electrons of Ru atoms were modeled using the SDD effective core pseudo-potential [65, 67]. The PBE0 functional was shown to be a reliable method in predicting both the properties and reactions involved with transition metals and metal clusters [68], including Ru, with accuracies approaching or exceeding other functionals commonly utilized in solid state systems [69].

Small molecule (i.e., nitrate, nitrite, and other reacting species) adsorption to the metal clusters were optimized at the PBE0/Lanl2DZ(Ru)/6-31+G(d,p)(H, N, O) level of theory. The geometry optimization of small molecules was performed with the Ru cluster fixed. Thermodynamic barriers were calculated from the bottom of the well energies, as thermodynamic corrections would be an unnecessary addition of error due to the frozen bond constraints given to the metal atom centers. The integral equation formalism polarizable continuum model (IEF-PCM) [70] was used to implicitly model the aqueous environment and was present in all optimizations and single point energy calculations. To correct for spin contamination for unpaired electron intermediates, single point energies utilizing a restricted open shell (RO) wavefunction were calculated at the ROPBE0/Lanl2DZ(Ru)/6-31+G(d,p)(H, N, O) level of theory. When multiple conformations of adsorbed N-containing species were possible, the complexes with the lowest energy were chosen for the calculation of reaction energies.

3. Results and discussion

3.1. Catalytic nitrate reduction

Fig. 1 shows the catalytic reduction of aqueous nitrate on Ru/C in comparison to monometallic Pd/C and bimetallic Pd-Cu/C. In contrast to an earlier report of limited nitrate reactivity with Ru catalysts [28], these experiments demonstrate that Ru is an effective catalyst, exhibiting much greater activity than monometallic Pd/C of the same mass loading and similar activity to Pd/C after immobilization of 1 wt% Cu as secondary promoter metal. For all three catalysts shown in Fig. 1, nitrate reduction kinetics follow a pseudo-first-order rate law over at least the first reaction half-life, and model fits of the data shown yield Ru- and Pd-mass-normalized pseudo-first-order rate constants of 4.13 ± 0.30 $L \cdot g_{Ru}^{-1} \cdot min^{-1}$, 0.46 ± 0.08 $L \cdot g_{Pd}^{-1} \cdot min^{-1}$, and 4.18 ± 0.01 $L \cdot g_{Pd}^{-1} \cdot min^{-1}$ for Ru/C, Pd/C, and Pd-Cu/C catalysts, respectively. The rate constants are calculated using the metal loading reported in Table 1. Control experiments conducted under continuous N_2 sparging (catalyst suspensions sparged with H_2 for 30 min followed by N_2 for another 60 min to displace H_2 before introducing nitrate to the reactor) show negligible loss of nitrate, demonstrating minimal adsorption onto the catalyst supports. Since the catalysts were subjected to the same *in situ* H_2 pre-reduction step before switching to N_2 sparging, this observation also indicates negligible direct reduction of nitrate by the metallic Ru or Pd phases. Initial rates of nitrate reduction vary linearly with catalyst loading between 0 and 0.5 $g \cdot L^{-1}$ Ru/C (Fig. S2), indicating that catalyst suspensions were well mixed and external mass transfer limitations for the reactants (nitrate and H_2) were insignificant under the studied conditions. The estimated Weisz-Prater parameter (C_{WP}) (SI Section

S5) is <<1, indicating that the internal mass transfer within the porous catalyst support particles is also not rate limiting. Ru/C exhibited good stability in batch re-use experiments, with activity decreasing <5% after each run (Fig. S3). Dissolved Ru measured in the supernatant of catalyst suspensions was below 1 ppb, demonstrating negligible leaching of the active metal. Electron microscopy of the catalyst collected following repeated re-use shows no agglomeration or growth of Ru nanoparticles (Fig. 3a and 3b). The small drop in activity observed between runs is speculated to be caused by material loss during the filtration recovery protocol used between runs. Immobilization of secondary promoter metals (1 wt% Cu and In) that have been reported to enhance nitrate reduction activity for Pd catalysts did not enhance Ru/C reactions with nitrate (data not shown).

Reductive transformation of nitrate, rather than adsorption or other transformation process, is also confirmed by the good nitrogen mass balance closure (Fig. 2a) observed using closed-bottle batch experiments with the aid of a ^{15}N-labeled nitrate salt that eliminated potential artifacts from atmospheric contamination during analysis of N_2. For Ru/C, nitrate is converted selectively to ammonium without producing any detectable $^{15}N_2$ by GC-MS analysis, and none of the transient aqueous or gaseous intermediates typically observed for Pd-based catalysts (nitrite and N_2O) [39, 71] are detected.

The effect of solution pH on nitrate reactions with Ru/C was evaluated in the open semi-batch systems using HCl/NaOH to maintain pH (Fig. S4). Ru-mass-normalized pseudo-first-order rate constants are relatively constant between pH 5-8, but decrease significantly at lower and higher pH conditions. Since gaseous nitrogen species cannot be measured in the open semi-batch reactors sparged

220 continuously with H_2, a stringent mass balance analysis of endproducts was not feasible. However,
221 ammonium product yields reached ≥90% of the initial nitrate concentrations for all pH conditions,
222 consistent with the high selectivity measured in the closed reactor experiment conducted at pH 5.5 using
223 ^{15}N-labeled species (Fig. 2a).

224 Comparison between metal dispersion and active surface in Table 1 suggests that 30 min of H_2
225 treatment at 25 ℃ is sufficient to re-reduce a large fraction of any surface oxides that might form upon
226 air passivation of *ex situ* H_2 pretreated catalysts. Despite the heterogeneity in particle morphology (Fig.
227 3 and Fig. S5) and an assumed 1:1 CO:Metal adsorption stoichiometry for all catalysts irrespective of
228 metal particle size and support, metal dispersion values derived from CO chemisorption analysis [73]
229 are reasonably consistent with particle sizes observed by electron microscopy (Table 1). The rate
230 constants for monometallic catalysts correspond to initial turnover frequencies (TOF_0) of 2.1 ± 0.2 min^{-1}
231 for Ru/C and 0.42 ± 0.07 min^{-1} for Pd/C based on active metal surface. TOF_0 of nitrate reduction on
232 Ru/C is five times greater than that of Pd/C. The higher reactivity of monometallic Ru/C than Pd/C is
233 especially noteworthy because the Pd/C reactivity observed in Fig. 1 is actually much greater than that
234 reported in earlier studies that found either no reaction with nitrate or a very low extent of reaction [30,
235 31, 56, 74-76]. Trawczyński *et al.* [71] calculated TOF_0 of nitrate reduction on an in-house prepared
236 Pd/C catalyst to be ~0.03 min^{-1}, which is one order-of-magnitude lower than the TOF_0 calculated from
237 data for Pd/C in Fig. 1. Considering that deionized water (⩾18 MΩ·cm^{-1}) was used for all experiments
238 and known promoter metals for Pd catalyst including Cu, In, and Sn were not detected by Energy

239 Dispersive X-ray spectroscopy analysis of Pd/C, we believe that the higher activity of Pd/C observed
240 here is not due to promoter metal contamination from solution or surface residues present following
241 synthesis of catalyst support.

242 The nature of active sites in Pd-Cu bimetallic catalysts is not well understood or characterized.
243 Although it is technically possible to estimate surface atoms by H_2 chemisorption [23, 77], we believe
244 the measurement does not represent bimetallic sites and chose not to calculate the TOF_0 for nitrate
245 reduction on Pd-Cu/C or compare the intrinsic activity between Ru and Pd-Cu bimetallic surface.
246 However, it can be seen from Table S1 that the Pd-Cu/C catalyst prepared for comparison in this study
247 exhibits activity on a Pd mass-normalized basis that is comparable with other studies that focused in
248 greater depth on the activity and mechanism of such bimetallic catalysts.

249 **3.2. Effect of pretreatment on nitrate reduction activity**

250 The high activity of Ru/C with nitrate observed here in comparison with earlier reports warrants
251 further examination. Several studies have documented that the reactivity of supported metal
252 nanoparticles is influenced by nanoparticle size and shape, chemical state, support properties and
253 metal-support interaction, which are subject to the starting materials (support material and metal
254 precursor), synthesis methods and activation steps [36, 78]. The present study used commercially
255 produced catalysts to take advantage of materials with optimized industrial production and adapted for
256 large scale applications. However, the high reactivity with aqueous nitrate of Ru catalysts was
257 demonstrated with the catalyst pretreated *ex situ* in flowing H_2 at 350 °C for 2 h prior to use, and the

as-received Ru/C and Ru/Al_2O_3 show low or no activity. To further characterize the effects of *ex situ* pretreatment on catalyst activity, we had commercial Ru/C, Ru/Al_2O_3, Pd/C and Pd/Al_2O_3 subjected to *ex situ* heat treatment (350 °C, 2 h) in both inert gas (N_2) and reducing gas (H_2) and tested of their nitrate reduction activity. The metal mass-normalized pseudo-first-order rate constants for nitrate reduction with these materials are calculated and presented in Fig. 4. *Ex situ* pretreatment of Ru/C, either with flowing H_2 or N_2, leads to more than a threefold increase in catalyst activity compared to the as-received catalyst. The effect of pretreatment is most pronounced for Ru/Al_2O_3, in that the catalyst is only active after pretreatment in flowing H_2. In comparison, pretreatment has no effect on the activity of Pd/C. Pd/Al_2O_3 exhibited no activity for nitrate reduction irrespective of catalyst pretreatment.

A battery of characterization analyses was conducted to rationalize the dramatic influence of *ex situ* pretreatment on Ru catalysts. XRD scan of Ru/C (Fig. 5a) shows mainly peaks associated with crystalline carbon phases, but no significant peaks for Ru metal (ca. 44° and 38°, JCPDS card No. 06-0663) or RuO_2 (ca. 28°, 35° and 54°, JCPDS card No. 43-1027), indicating small crystal size below XRD detection limit. The XRD pattern for Ru/Al_2O_3 (Fig. 5b) shows crystalline RuO_2 in both the as-received and *ex situ* N_2 pretreated materials, but these features disappear and new features characteristic of crystalline Ru metal appear in the H_2 pretreated Ru/Al_2O_3. For both Ru/C and Ru/Al_2O_3 catalysts, the catalyst activity (Fig. 4) roughly correlates with the active Ru surface of catalysts (Table S2), suggesting that catalyst pretreatment increased the Ru surface area active for catalytic reaction.

Increasing surface area often results from decreased particle size, which is not the case for Ru/C in this study. The size distribution of Ru particles in the as-received Ru/C (1.9 ± 0.6 nm, Fig. 3c) is not statistically different from that measured following the *ex situ* H_2 pretreatment process (2.2 ± 0.8 nm, Fig. 3a). Another possibility is that the Ru catalyst surface in the as-received Ru/C is blocked by residues from synthesis, which may be partially or fully removed by the high temperature pretreatment processes. H_2 TPR analysis provides evidence to support this hypothesis. The TPR profiles (Fig. 6) of *ex situ* H_2- and N_2-pretreated Ru/C are similar, with a first reduction peak located between 50 and 55 °C and a second broad reduction peak above 400 °C. The reduction peak temperature of supported Ru oxides formed during catalyst calcination has been reported to vary between 65 °C and 185 °C [79, 80]. Though the temperature of the first reduction peak observed here falls below this range, the H_2 consumption quantified from the peak area (Table S2) is consistent with the theoretical stoichiometry for H_2 consumption during RuO_2 reduction [79]:

$$RuO_2 + 2H_2 \rightarrow Ru + 2H_2O \quad (3)$$

The Ru oxides formed upon re-oxidation of pretreated Ru upon exposure to ambient air are redox-labile, enabling re-reduction by H_2 at 25 °C. The second reduction peak is assigned to the direct reduction of aldehyde, quinone and phenol groups on the carbon support [81]. The TPR profile for as-received Ru/C is markedly different from those of *ex situ* pretreated Ru/C. A much larger H_2 consumption and a dip in the TCD signal match the features of surface species decomposition and desorption, supporting the hypothesis that the as-received catalyst surface is blocked by residues that desorb upon heat pretreatment.

Temperature-programmed desorption study of as-received Ru/C and *ex situ* H_2 pretreated Ru/C in Ar provides further confirmation of surface species desorption at 47 ℃ for as-received Ru/C (Fig. S6). Therefore, as-received Ru/C consists of highly reducible Ru oxides that are covered by surface contaminants. The *ex situ* pretreatment of Ru/C increased catalyst activity mainly by removing these surface contaminants while causing minimal effect on Ru oxides particles.

The as-received Ru/Al_2O_3 and *ex situ* N_2 pretreated Ru/Al_2O_3 exhibit a TPR pattern consistent with RuO_2 reduction reported in the literature, which is also in agreement with the crystalline RuO_2 identified by XRD analysis. Although the stoichiometry for H_2 consumption of RuO_2 in these two Ru/Al_2O_3 catalysts is similar to that of RuO_2 in *ex situ* H_2- and N_2-pretreated Ru/C (Table S2), the Ru oxides on the two supports show significant differences in reducibility as evidenced by the much lower reduction peak temperature of Ru/C catalysts. Besides, the surface of RuO_2 in *ex situ* H_2- and N_2-pretreated Ru/C is easily reduced by H_2 at 25 ℃, while the surface of RuO_2 in as-received Ru/Al_2O_3 and *ex situ* N_2 pretreated Ru/Al_2O_3 is not reducible with H_2 at 25 ℃ (Table S2). In contrast, *ex situ* H_2 pretreated Ru/Al_2O_3 shows a small H_2 consumption peak at 45 ℃, similar to the highly reducible RuO_2 in *ex situ* H_2- and N_2-pretreated Ru/C and consistent with crystalline metallic Ru in *ex situ* H_2 pretreated Ru/Al_2O_3 identified by XRD analysis. Based on these observations, it can be concluded that *ex situ* H_2 pretreatment activates Ru/Al_2O_3 by reducing the crystalline RuO_2 to a metallic Ru phase, whose surface is re-oxidized upon exposure to ambient temperature air to a more redox-labile form of RuO_2 (e.g., less crystalline) that can be re-reduced by H_2 at 25 ℃. A complete re-oxidation of pretreated Ru/C compared

313 with partial re-oxidation of H_2 pretreated Ru/Al_2O_3 is attributed to a much smaller size of Ru
314 nanoparticles in Ru/C than in Ru/Al_2O_3. The *ex situ* N_2 pretreatment fails to activate Ru/Al_2O_3 due to the
315 inability of N_2 to transform crystalline RuO_2 to redox-labile species. Therefore, it is further confirmed
316 that redox-labile surface Ru oxides are essential to achieve good performance in catalytic nitrate
317 reduction applications.

318 **3.3. Catalytic nitrite reduction**

319 Based on the prevailing mechanism for nitrate reduction with Pd-based catalysts, the first reduction
320 intermediate is anticipated to be nitrite [32, 82, 83], and the fact that no nitrite intermediate is observed
321 when monitoring nitrate reactions (Fig. 2a) would suggest nitrite reduction is much faster than nitrate
322 reduction at comparable conditions (similar to observations reported for Pd catalysts under most
323 conditions [31, 74, 84]). Compared to nitrate, reduction of nitrite is less well described by a
324 pseudo-first-order rate law, with the reaction appearing to accelerate as nitrite concentration continues to
325 drop after the first two half-lives (Fig. 7a). Nevertheless, the pseudo-first-order rate constants for nitrite
326 reduction over the first two half-lives was calculated to provide a rough measure of catalyst activity to
327 compare with that measured for nitrate reduction under similar conditions. Surprisingly, the observed
328 reaction kinetics for nitrite are markedly slower than for nitrate under the same conditions. The
329 mass-normalized pseudo-first-order rate constant for nitrite reduction derived from the model fit of data
330 in Fig. 7a is 1.44 ± 0.15 $L \cdot g_{Ru}^{-1} \cdot min^{-1}$, corresponding to an TOF_0 of 0.73 ± 0.06 min^{-1}. This value is
331 about one third of the TOF_0 for nitrate measured under the same conditions (2.1 ± 0.2 min^{-1}). The lower

activity of nitrite in comparison to nitrate contrasts with typical results reported for Pd-based bimetallic catalysts, where nitrite is much more reactive than the parent nitrate ion [39, 74]. Nitrite reaction with Pd/C at the same conditions shown in Fig. 7a yields a TOF_0 of 57.7 ± 9.2 min^{-1}.

The isotope labeling mass balance closure experiment conducted with nitrite as a starting reactant (Fig. 2b) further reveals a distinct behavior of Ru-catalyzed nitrite reduction. In contrast to the experiment initiated with nitrate, nitrite reduction yields a mixture of N_2 and ammonium endproducts, and N_2O is observed as a reaction intermediate. Whereas the sole product of nitrate reduction detected is ammonium irrespective of initial nitrate concentration (Fig. 8a), the distribution of N_2:ammonium observed in nitrite reduction experiments shifts increasingly towards N_2 with increasing initial nitrite concentration (Fig. 8b).

3.4. Site-limited reduction kinetics

As mentioned earlier, measured nitrite concentrations drop below pseudo-first-order kinetic model predictions as the reaction progresses and nitrite concentration decreases (Fig. 7a). To examine this further, TOF_0 of nitrate and nitrite reduction were determined at varying initial concentration of each oxyanion. Results of these measurements (Fig. 7b) reveal contrasting behavior for nitrate and nitrite. For nitrate, the observed trend is consistent with the classical Langmuir-Hinshelwood model for heterogeneous reactions, where TOF_0 increases with increasing initial nitrate concentration until it approaches a maximum value due to saturation of available surface reaction sites [86]. Similar behavior has been documented for many heterogeneous catalytic reactions, including nitrate, nitrite, and bromate

351 reactions with Pd-based catalyst [33, 87, 88]. The small drop in TOF_0 observed at the highest initial
352 nitrate concentration tested may result from competitive adsorption between nitrate and H_2 on the same
353 reaction sites [89]. A contrasting and atypical behavior is observed for nitrite, where TOF_0 values are
354 greatest at the lowest initial nitrite concentration and decrease to minimum value with increasing nitrite
355 concentration. To rationalize this trend within the framework of a Langmuir-Hinshelwood model
356 requires an assumption that nitrite competes directly with H_2 for the same reaction sites and the former
357 has a much higher affinity for the sites than the latter, thereby inhibiting uptake and dissociation of the
358 required H_2 reductant at higher nitrite concentrations. An important implication of this finding is that the
359 relative reactivities observed for nitrate versus nitrite (e.g., Fig. 7a) are heavily dependent upon the
360 initial oxyanion concentrations used in the reactions. The heightened reactivity of nitrite at low nitrite
361 concentrations can also potentially explain why the species is not observed as a reaction intermediate
362 during Ru catalyst reactions initiated with nitrate; when nitrite is formed at low concentrations on the
363 catalyst surface, its rapid turnover under these conditions prevents detection in the overlying aqueous
364 solution. The competition between nitrite and H_2 adsorption may also contribute to the observed shift in
365 endproduct selectivity towards ammonium at lower initial nitrite concentration (Fig. 8b); conversion of
366 nitrite to ammonium has a relatively higher stoichiometric requirement for H_2 than reduction to N_2, so
367 an increase in H_2:nitrite ratio could favor the pathway for ammonium production by increasing surface
368 coverage of hydrogen and decreasing surface coverage of nitrogen species. The decreasing nitrite

369 concentration is also expected to reduce the rate of N-N pairing reactions necessary to N_2O and N_2.
370 Detailed pathways will be discussed in the following section.

371 Since separate reactions conducted with nitrate and nitrate suggest that the oxyanions both compete
372 with H_2 for chemisorption at Ru active sites, competitive reactions between the two oxyanions were
373 further examined by reaction initiated with mixtures of nitrate and nitrite. Fig. 7c shows the reaction of
374 an equimolar mixture of nitrate and nitrite at the same conditions as the individual oxyanion reactions
375 shown in Fig. 7a. Interestingly, despite the fact that nitrite reacts slower than nitrate when the two
376 oxyanions are reacted with Ru/C separately, the presence of nitrite severely inhibits nitrate reduction.
377 Nitrate reduction kinetics proceeds in two phases. A severely inhibited reduction phase is observed
378 while nitrite is present, but the reaction accelerates once the nitrite is fully depleted. Variation of the
379 ratio of initial nitrate and nitrite confirmed competition between the two oxyanions for available
380 catalysts reaction sites, since the initial rate of nitrate reduction in the first phase increases with
381 increasing nitrate/nitrite ratio, which is the same case for nitrite reduction measured in the presence of
382 nitrate (Table S3).

383 **3.5. Proposed reaction pathway**

384 Ru catalysts behave differently from Pd-based catalysts in nitrate reduction product selectivity. For
385 example, Ru catalysts favor complete selectivity for ammonium (Fig. 2a), in contrast with a mixture of
386 ammonium and N_2 endproducts reported for Pd-based bimetallic catalysts [23, 31]. Consistently high
387 (and possibly complete) selectivity for ammonium was observed for Ru catalysts under various solution

388 pH, whereas the ratio between ammonium and N_2 varies with shifting pH conditions for Pd-based
389 bimetallic catalysts [31, 41, 72]. On the other hand, Ru catalysts and Pd-based catalysts share similarity
390 in nitrite reduction product selectivity. For Ru/C, the distribution of N_2:ammonium shifts increasingly
391 towards N_2 with increasing initial nitrite concentration (Fig. 8b), similar to trends reported for Pd-based
392 catalysts [85]. Scheme 1 depicts the generally accepted mechanism of nitrate reduction on Pd-based
393 catalysts. The experimental observations of nitrite reduction with Ru catalysts appear to be consistent
394 with the reaction pathways proposed for Pd-based catalysts. Reactions initiated with nitrite yield
395 transient intermediates and endproducts consistent with the two parallel pathways for NO reduction (Fig.
396 2b). It may not be straightforward to apply the scheme to nitrate reduction with Ru catalysts considering
397 the differences mentioned above and that reactions initiated with nitrate show no detectable nitrite
398 intermediate (Fig. 2a). However, the lack of observed nitrite intermediate is consistent with the elevated
399 turnover rate of this species observed at low initial concentrations (Fig. 7b) and selective reactivity of
400 nitrite in the presence of nitrate (Fig. 7c). Along this line, the complete selectivity for ammonium is
401 possibly a result of high selectivity to ammonium at low nitrite concentration (Fig. 8b).

402 It should be pointed out that Scheme 1 only provides a macroscopic picture for the reaction. When
403 considering the reaction from the microscopic viewpoint, the mechanism involves much more diverse
404 intermediates that are adsorbed on the surface or in the aqueous phase. To obtain molecular insights into
405 the mechanism of the reaction over Ru, DFT calculations were conducted to evaluate the
406 thermodynamics of adsorption and transformation steps. Adsorption energies and conformations of

major reactants, hypothesized intermediates and products are provided in SI Table S4. The elementary steps underlying the reaction pathways in Scheme 1 are illustrated in Fig. 9, and the energetics of each step are listed in Table S5. The strong adsorption of NO_2^- (-1.3 eV) and NO (-2.0 eV) from water to the Ru cluster surface may be contributing to the fact that desorbed aqueous species of the latter two were never observed during reactions initiated with nitrate. The further sequential reduction of NO_{ads} to $NH_{3,ads}$ occurs through a series of exothermic reaction steps. Previous observations of the complete selectivity for ammonium in reactions initiated with nitrate (Fig. 8a) and the shift in endproduct selectivity towards N_2 for nitrite reactions conducted with higher initial aqueous concentrations (Fig. 8b) indicate that buildup of aqueous nitrite concentrations is a prerequisite for the reaction pathway leading to diatomic nitrogen species. We found that initiating N-N coupling by reaction of the NO_{ads} intermediate with aqueous nitrite is exothermic, and subsequent reduction of the resulting intermediate to form both the detectable N_2O intermediate and stable N_2 endproduct are also favorable. Some have proposed that NO_{ads} dissociates first to N_{ads} and O_{ads} on catalyst metal surfaces before reacting further to form the observed products [30, 85]. DFT calculations indicate that this route cannot be ruled out based on energetics, but coupling between N_{ads} and NO_{ads} is unfavorable. The findings from DFT calculations that both reaction pathways are thermodynamically favorable implies that the kinetic factors, rather than thermodynamic constraints, are likely responsible for controlling the reaction product selectivity. Calculations of kinetic properties will be needed to provide further insights into the reaction rates and endproduct selectivities observed in experiments.

3.6. Implications for technology development

Results of this study demonstrate that Ru catalysts effectively reduce nitrate at ambient temperature and H_2 pressure. Ru possesses many of the benefits of other Pt group metal catalysts (e.g., high stability) but is less expensive than Pd and Pt, showing potential to reduce barriers to catalyst technology adoption for treatment of recalcitrant water contaminants. The reductant (H_2) is low cost, can be generated on-site electrochemically, and has lower life-cycle environmental impacts than organic electron donors typically used in biological denitrification processes [24]. The catalysts used in the study are a commercially available material from a vendor capable to high volume production, making the process accessible to near-term commercial applications. The sole endproduct from nitrate reduction by the supported Ru catalysts investigated was ammonium, indicating that Ru catalysts are not suitable for treating drinking water with dilute nitrate in a single process. On the other hand, highly selective conversion of nitrate to ammonium, especially in concentrate matrices like waste ion exchange regenerant brines [90], if followed by separation unit processes (e.g., membrane electrolysis [91]), may be a promising strategy for sustainably recovering an economically valuable product (e.g., $(NH_4)_2SO_4$), which is in line with a growing interest in resource recovery from waste streams [92]. A number of technology development challenges remain to demonstrate viability, safety, and to de-risk the technology, but findings in this study suggest a path forward for development of an economical and sustainable technology for treatment and resource recovery from nitrate-contaminated water sources.

Rational design that emphasizes "design-for-purpose" is important to advance next-generation water treatment technologies [93]. Pt group metals are known to activate H_2. In order to couple H_2 oxidation with nitrate reduction, the activity of nitrate activation on Ru and the steps controlling selectivity need to be understood and is the objective of this study. Examination of the reaction mechanism revealed that selectivity for N_2 endproduct is limited during nitrate reduction with the Ru catalyst formulations examined here because N-N coupling requires significant aqueous nitrite concentrations to buildup and pairing between adsorbed N species is negligible. This suggests a target for future Ru catalyst design: tailor active sites for selective adsorption with nitrate over nitrite and/or reducing barriers to mobility and pairing of adsorbed N species. Surface alloying may be used to alter small molecule binding strength and rates of surface species diffusion [94, 95]. Alternatively, bio-inspired catalyst structures that attempt to mimic the multi-component features and activated metalloenzyme centers of biological systems may offer a promising strategy for enhancing catalyst activity. For example, Liu and co-workers recently demonstrated >100-fold improvement in catalytic reduction of the recalcitrant oxyanion perchlorate by modifying the Re component within Pd-Re/C bimetallic catalysts by complexing with oxazoline ligands that enhance the metal's oxygen atom transfer (OAT) reactivity [96], mimicking the design of Mo-centered OAT metal complexes in the perchlorate reductase enzyme. Inspired by the heme-containing active sites of nitrate and (per)chlorate reductase, Ford and co-workers constructed a non-heme iron complex for catalytic nitrate and perchlorate reduction, and the homogeneous catalyst is

462 regenerated by electrons and protons provided by 1,2-diphenylhydrazine [97]. Biomimetic catalysts
463 incorporating Ru as the active metal center for nitrate or nitrite reduction have not been reported to date.

464 ## 4. Conclusions

465 Supported Ru nanoparticles showed promising catalytic performance in reducing nitrate in water at
466 ambient temperature and H_2 pressure. It is demonstrated that Ru has a high intrinsic activity in nitrate
467 activation, which is five times higher than that of Pd under standard testing conditions. The key features
468 for supported Ru catalysts that need to be controlled to achieve high activity are that reduced Ru surface
469 can be obtained by H_2 reduction at reaction temperature and that the surface is not blocked by synthesis
470 residues. Ru reduces nitrate selectively to ammonium, while nitrite is reduced to yield a mixture of N_2
471 and ammonium, with selectivity shifting towards N_2 at increasing nitrite:hydrogen ratio. The reaction
472 mechanism is proposed that sequential hydrogenation of nitrate to nitrite and NO is followed by parallel
473 pathways involving the adsorbed NO: (1) sequential hydrogenation to ammonium, and (2) N-N coupling
474 with aqueous nitrite followed by hydrogenation to the detected N_2O intermediate and N_2 endproduct.
475 Future work is needed to strategically design catalyst to control selectivity and develop integrated
476 processes for nitrogen recovery.

477 **Acknowledgements**

478 This work was supported by the National Science Foundation (CBET-1555549) and the U.S. EPA
479 Science to Achieve Results Program (#RD83517401). Computational resources from High Performance
480 Computing facility at CSM are gratefully acknowledged. We thank Ryan Richards, Martin Menart and

Mengze Xu (CSM) for access and assistance with gas adsorption measurements. We thank David Diercks (CSM) for assistance with STEM analysis. Charles Werth (Univ. Texas), Danmeng Shuai (George Washington Univ.) and Yun Shen (Univ. of Illinois) are also acknowledged for their advice and helpful discussions.

References

[1] R.F. Spalding, M.E. Exner, J. Environ. Qual., 22 (1993) 392-402.
[2] A. Kapoor, T. Viraraghavan, J. Environ. Eng.-ASCE, 123 (1997) 371-380.
[3] L.J. Puckett, Environ. Sci. Technol., 29 (1995) 408A-414A.
[4] A. Pintar, Catal. Today, 77 (2003) 451-465.
[5] P.J. Weyer, J.R. Cerhan, B.C. Kross, G.R. Hallberg, J. Kantamneni, G. Breuer, M.P. Jones, W. Zheng, C.F. Lynch, Epidemiology, 12 (2001) 327-338.
[6] G. Gulis, M. Czompolyova, J.R. Cerhan, Environ. Res., 88 (2002) 182-187.
[7] J.K. Choe, A.M. Bergquist, S. Jeong, J.S. Guest, C.J. Werth, T.J. Strathmann, Water Res., 80 (2015) 267-280.
[8] S. Samatya, N. Kabay, U. Yuksel, M. Arda, M. Yuksel, React. Funct. Polym., 66 (2006) 1206-1214.
[9] J. Bohdziewicz, M. Bodzek, E. Wasik, Desalination, 121 (1999) 139-147.
[10] A. El Midaoui, F. Elhannouni, M. Taky, L. Chay, M.A.M. Sahli, L. Echihabi, M. Hafsi, Sep. Purif. Technol., 29 (2002) 235-244.
[11] F. Hell, J. Lahnsteiner, H. Frischherz, G. Baumgartner, Desalination, 117 (1998) 173-180.
[12] B.-U. Bae, Y.-H. Jung, W.-W. Han, H.-S. Shin, Water Res., 36 (2002) 3330-3340.
[13] N. Barrabés, J. Sá, Appl. Catal., B, 104 (2011) 1-5.
[14] M. Shrimali, K.P. Singh, Environ. Pollut., 112 (2001) 351-359.
[15] I. Mikami, Y. Yoshinaga, T. Okuhara, Appl. Catal., B, 49 (2004) 173-179.
[16] C.-P. Huang, H.-W. Wang, P.-C. Chiu, Water Res., 32 (1998) 2257-2264.
[17] A.P. Murphy, Nature, 350 (1991) 223-225.
[18] M. Kumar, S. Chakraborty, J. Hazard. Mater., 135 (2006) 112-121.
[19] F. Gauthard, F. Epron, J. Barbier, J. Catal., 220 (2003) 182-191.
[20] B.P. Chaplin, E. Roundy, K.A. Guy, J.R. Shapley, C.J. Werth, Environ. Sci. Technol., 40 (2006) 3075-3081.
[21] I. Dodouche, D.P. Barbosa, M.d.C. Rangel, F. Epron, Appl. Catal., B, 93 (2009) 50-55.
[22] R. Zhang, D.M. Shuai, K.A. Guy, J.R. Shapley, T.J. Strathmann, C.J. Werth, ChemCatChem, 5 (2013) 313-321.

514 [23] S. Jung, S. Bae, W. Lee, Environ. Sci. Technol., 48 (2014) 9651-9658.
515 [24] J.K. Choe, M.H. Mehnert, J.S. Guest, T.J. Strathmann, C.J. Werth, Environ. Sci. Technol., 47
516 (2013) 4644-4652.
517 [25] U. Prüsse, K.-D. Vorlop, J. Mol. Catal. A: Chem., 173 (2001) 313-328.
518 [26] J. Jung, S. Bae, W. Lee, Appl. Catal., B, 127 (2012) 148-158.
519 [27] S. Hörold, T. Tacke, K.D. Vorlop, Environ. Technol., 14 (1993) 931-939.
520 [28] O. Soares, J.J.M. Orfao, M.F.R. Pereira, Catal. Lett., 126 (2008) 253-260.
521 [29] D. Shuai, J.K. Choe, J.R. Shapley, C.J. Werth, Environ. Sci. Technol., 46 (2012) 2847-2855.
522 [30] O.M. Ilinitch, L.V. Nosova, V.V. Gorodetskii, V.P. Ivanov, S.N. Trukhan, E.N. Gribov, S.V.
523 Bogdanov, F.P. Cuperus, J. Mol. Catal. A: Chem., 158 (2000) 237-249.
524 [31] Y. Yoshinaga, T. Akita, I. Mikami, T. Okuhara, J. Catal., 207 (2002) 37-45.
525 [32] U. Prüsse, M. Hähnlein, J. Daum, K.-D. Vorlop, Catal. Today, 55 (2000) 79-90.
526 [33] A. Pintar, J. Batista, J. Levec, T. Kajiuchi, Appl. Catal., B, 11 (1996) 81-98.
527 [34] A. Pintar, J. Batista, I. Arčon, A. Kodre, Characterization of γ-Al2O3 supported Pd-Cu bimetallic
528 catalysts by EXAFS, AES and kinetic measurements, in: B. Delmon, P.A. Jacobs, R. Maggi, J.A.
529 Martens, P. Grange, G. Poncelet (Eds.) Stud. Surf. Sci. Catal., Elsevier, Louvain-la-Neuve, Belgium,
530 1998, pp. 127-136.
531 [35] F.A. Marchesini, S. Irusta, C. Querini, E. Miró, Appl. Catal., A, 348 (2008) 60-70.
532 [36] A. Miyazaki, K. Matsuda, F. Papa, M. Scurtu, C. Negrila, G. Dobrescu, I. Balint, Catal. Sci.
533 Technol., 5 (2015) 492-503.
534 [37] S. Bae, J. Jung, W. Lee, Chem. Eng. J., 232 (2013) 327-337.
535 [38] S. Hörold, K.D. Vorlop, T. Tacke, M. Sell, Catal. Today, 17 (1993) 21-30.
536 [39] K.A. Guy, H. Xu, J.C. Yang, C.J. Werth, J.R. Shapley, J. Phys. Chem. C, 113 (2009) 8177-8185.
537 [40] X. Fan, C. Franch, E. Palomares, A.A. Lapkin, Chem. Eng. J., 175 (2011) 458-467.
538 [41] G. Centi, S. Perathoner, Appl. Catal., B, 41 (2003) 15-29.
539 [42] F.X. Zhang, S. Miao, Y.L. Yang, X. Zhang, J.X. Chen, N.J. Guan, J. Phys. Chem. C, 112 (2008)
540 7665-7671.
541 [43] Z. Xu, L. Chen, Y. Shao, D. Yin, S. Zheng, Ind. Eng. Chem. Res., 48 (2009) 8356-8363.
542 [44] M. D'Arino, F. Pinna, G. Strukul, Appl. Catal., B, 53 (2004) 161-168.
543 [45] H.Y. Chen, S.L. Lo, H.H. Ou, Appl. Catal., B, 142 (2013) 65-71.
544 [46] F. Epron, F. Gauthard, C. Pinéda, J. Barbier, J. Catal., 198 (2001) 309-318.
545 [47] http://www.platinum.matthey.com/prices/price-charts. (accessed 01/07, 2017)
546 [48] R. Brunet Espinosa, L. Lefferts, ACS Catal., 6 (2016) 5432-5440.
547 [49] http://www.infomine.com/investment/metal-prices/nickel/. (accessed 01/07, 2017)
548 [50] L. Calvo, M.A. Gilarranz, J.A. Casas, A.F. Mohedano, J.J. Rodriguez, Ind. Eng. Chem. Res., 49
549 (2010) 5603-5609.
550 [51] B.P. Chaplin, M. Reinhard, W.F. Schneider, C. Schuth, J.R. Shapley, T.J. Strathmann, C.J. Werth,
551 Environ. Sci. Technol., 46 (2012) 3655-3670.

[52] J. Petró, A. Bóta, K. László, H. Beyer, E. Kálmán, I. Dódony, Appl. Catal., A, 190 (2000) 73-86.
[53] L. Chen, Y. Zhu, H. Zheng, C. Zhang, B. Zhang, Y. Li, J. Mol. Catal. A: Chem., 351 (2011) 217-227.
[54] T. Yoneda, T. Takido, K. Konuma, Appl. Catal., B, 84 (2008) 667-677.
[55] G.E. Dima, A.C.A. de Vooys, M.T.M. Koper, J. Electroanal. Chem., 554–555 (2003) 15-23.
[56] X. Chen, X. Huo, J. Liu, Y. Wang, C.J. Werth, T.J. Strathmann, Chem. Eng. J., 313 (2017) 745-752.
[57] L. Lemaignen, C. Tong, V. Begon, R. Burch, D. Chadwick, Catal. Today, 75 (2002) 43-48.
[58] S.-F. Yin, Q.-H. Zhang, B.-Q. Xu, W.-X. Zhu, C.-F. Ng, C.-T. Au, J. Catal., 224 (2004) 384-396.
[59] F.R. García-García, A. Guerrero-Ruiz, I. Rodríguez-Ramos, Top. Catal., 52 (2009) 758-764.
[60] R. Sander, Compilation of Henry's Law Constants for Inorganic and Organic Species of Potential Importance in Environmental Chemistry. http://www.henrys-law.org (accessed July 2016).
[61] Gaussian 09, Revision C.01, M.J. Frisch, G.W. Trucks, H.B. Schlegel, G.E. Scuseria, M.A. Robb, J.R. Cheeseman, G. Scalmani, V. Barone, B. Mennucci, G.A. Petersson, H. Nakatsuji, M. Caricato, X. Li, H.P. Hratchian, A.F. Izmaylov, J. Bloino, G. Zheng, J.L. Sonnenberg, M. Hada, M. Ehara, K. Toyota, R. Fukuda, J. Hasegawa, M. Ishida, T. Nakajima, Y. Honda, O. Kitao, H. Nakai, T. Vreven, J.A. Montgomery Jr, J.E. Peralta, F. Ogliaro, M.J. Bearpark, J. Heyd, E.N. Brothers, K.N. Kudin, V.N. Staroverov, R. Kobayashi, J. Normand, K. Raghavachari, A.P. Rendell, J.C. Burant, S.S. Iyengar, J. Tomasi, M. Cossi, N. Rega, N.J. Millam, M. Klene, J.E. Knox, J.B. Cross, V. Bakken, C. Adamo, J. Jaramillo, R. Gomperts, R.E. Stratmann, O. Yazyev, A.J. Austin, R. Cammi, C. Pomelli, J.W. Ochterski, R.L. Martin, K. Morokuma, V.G. Zakrzewski, G.A. Voth, P. Salvador, J.J. Dannenberg, S. Dapprich, A.D. Daniels, Ö. Farkas, J.B. Foresman, J.V. Ortiz, J. Cioslowski, D.J. Fox, Gaussian, Inc., Wallingford, CT, USA, 2009.
[62] F. Aguilera-Granja, L.C. Balbás, A. Vega, J. Phys. Chem. A, 113 (2009) 13483-13491.
[63] W. Zhang, H. Zhao, L. Wang, J. Phys. Chem. B, 108 (2004) 2140-2147.
[64] C. Adamo, V. Barone, J. Chem. Phys., 110 (1999) 6158-6170.
[65] H.T. Dunning, Jr., P.J. Hay, Gaussian basis sets for molecular calculations, in: Schaefer, H. F. (Ed.), Methods of Electronic Structure Theory, Springer: New York, 1977, pp. 1-27.
[66] P.J. Hay, W.R. Wadt, J. Chem. Phys., 82 (1985) 299-310.
[67] D. Andrae, U. Häußermann, M. Dolg, H. Stoll, H. Preuß, Theor. Chim. Acta, 77 (1990) 123-141.
[68] M.M. Quintal, A. Karton, M.A. Iron, A.D. Boese, J.M.L. Martin, J. Phys. Chem. A, 110 (2006) 709-716.
[69] P. Janthon, S. Luo, S.M. Kozlov, F. Viñes, J. Limtrakul, D.G. Truhlar, F. Illas, J. Chem. Theory. Comput., 10 (2014) 3832-3839.
[70] J. Tomasi, B. Mennucci, E. Cancès, J. Mol. Struc.-THEOCHEM, 464 (1999) 211-226.
[71] J. Trawczyński, P. Gheek, J. Okal, M. Zawadzki, M.J.I. Gomez, Appl. Catal., A, 409–410 (2011) 39-47.
[72] B. Chaplin, J. Shapley, C. Werth, Catal. Lett., 130 (2009) 56-62.

590 [73]Micromeritics. (2009). Retrieved from
591 http://www.micromeritics.com/repository/files/autochem_ii_2920_operator_manual_v4.00.pdf.
592 [74] F. Deganello, L.F. Liotta, A. Macaluso, A.M. Venezia, G. Deganello, Appl. Catal., B, 24 (2000)
593 265-273.
594 [75] A. Garron, F. Epron, Water Res., 39 (2005) 3073-3081.
595 [76] J. Sá, H. Vinek, Appl. Catal., B, 57 (2005) 247-256.
596 [77] M.P. Maia, M.A. Rodrigues, F.B. Passos, Catal. Today, 123 (2007) 171-176.
597 [78] D. Shuai, D.C. McCalman, J.K. Choe, J.R. Shapley, W.F. Schneider, C.J. Werth, ACS Catal., 3
598 (2013) 453-463.
599 [79] S. Hosokawa, H. Kanai, K. Utani, Y.-i. Taniguchi, Y. Saito, S. Imamura, Appl. Catal., B, 45 (2003)
600 181-187.
601 [80] W. Deng, X. Tan, W. Fang, Q. Zhang, Y. Wang, Catal. Lett., 133 (2009) 167-174.
602 [81] S. Kundu, Y. Wang, W. Xia, M. Muhler, J. Phys. Chem. C, 112 (2008) 16869-16878.
603 [82] F. Epron, F. Gauthard, J. Barbier, J. Catal., 206 (2002) 363-367.
604 [83] A.O. Costa, L.S. Ferreira, F.B. Passos, M.P. Maia, F.C. Peixoto, Appl. Catal., A, 445–446 (2012)
605 26-34.
606 [84] S. Hamid, M.A. Kumar, W. Lee, Appl. Catal., B, 187 (2016) 37-46.
607 [85] H. Shin, S. Jung, S. Bae, W. Lee, H. Kim, Environ. Sci. Technol., 48 (2014) 12768-12774.
608 [86] M.A. Vannice, Kinetics of Catalytic Reactions, Springer, New York, 2005.
609 [87] J.K. Chinthaginjala, L. Lefferts, Appl. Catal., B, 101 (2010) 144-149.
610 [88] H. Chen, Z. Xu, H. Wan, J. Zheng, D. Yin, S. Zheng, Appl. Catal., B, 96 (2010) 307-313.
611 [89] L.E. Knitt, J.R. Shapley, T.J. Strathmann, Environ. Sci. Technol., 42 (2008) 577-583.
612 [90] A.M. Bergquist, J.K. Choe, T.J. Strathmann, C.J. Werth, Water Res., 96 (2016) 177-187.
613 [91] J. Desloover, A. Abate Woldeyohannis, W. Verstraete, N. Boon, K. Rabaey, Environ. Sci. Technol.,
614 46 (2012) 12209-12216.
615 [92] P. Kuntke, K.M. Śmiech, H. Bruning, G. Zeeman, M. Saakes, T.H.J.A. Sleutels, H.V.M. Hamelers,
616 C.J.N. Buisman, Water Res., 46 (2012) 2627-2636.
617 [93] R. Li, L. Zhang, P. Wang, Nanoscale, 7 (2015) 17167-17194.
618 [94] S. St. John, R.W. Atkinson, R.R. Unocic, T.A. Zawodzinski, A.B. Papandrew, J. Phys. Chem. C,
619 119 (2015) 13481-13487.
620 [95] A.U. Nilekar, J. Greeley, M. Mavrikakis, Angew. Chem. Int. Ed., 45 (2006) 7046-7049.
621 [96] J. Liu, J.K. Choe, Y. Wang, J.R. Shapley, C.J. Werth, T.J. Strathmann, ACS Catal., (2014)
622 511-522.
623 [97] C.L. Ford, Y.J. Park, E.M. Matson, Z. Gordon, A.R. Fout, Science, 354 (2016) 741-743.

Captions

Scheme 1. Nitrate hydrogenation pathway on Pd-based bimetallic catalysts

Fig. 1. Measured reaction timecourses for nitrate reduction and first-order model fits on 5 wt% Ru/C, 5 wt% Pd/C, and 5 wt% Pd-1 wt% Cu/C in the semi-batch reactor system (0.2 $g \cdot L^{-1}$ catalyst, $[NO_3^-]_0$ = 1.6 mM, 1 atm H_2 continuous sparging except in control experiments where 1 atm N_2 continuous sparging was used, pH 5.0 maintained by pH stat, 25 ± 0.5°C). Error bars represent standard deviations of triplicate reactions.

Table 1. Properties of catalysts used for nitrate activity test

Fig. 2. Timecourses showing aqueous and gaseous intermediates and products during Ru/C-catalyzed reduction of ^{15}N-labeled (a) nitrate and (b) nitrite monitored in closed-bottle batch systems (0.2 $g \cdot L^{-1}$ catalyst, $[^{15}NO_3^-]_0$ or $[^{15}NO_2^-]_0$ = 1.6 mM , initially 1 atm H_2, pH 5.5 buffered by 40 mM MES, 21 ± 1°C). Error bars represent standard deviations of triplicate reactions (smaller than symbol if not visible).

Fig. 3. HAADF-STEM images of (a) *ex situ* H_2 pretreated Ru/C, (b) Ru/C after re-use experiment, (c) as-received Ru/C and (d) *ex situ* H_2 pretreated Ru/Al_2O_3. The insets show Ru particle size distributions.

Fig. 4. Influence of catalyst pretreatments (as-received catalyst or *ex situ* pretreated in flowing H_2 or N_2 at 350 °C for 2 h) on reactivity with aqueous nitrate (0.2 $g \cdot L^{-1}$ catalyst with nominal 5 wt% Ru or Pd, $[NO_3^-]_0$ = 1.6 mM, 1 atm H_2 continuous sparging, pH 5.0 maintained by automatic pH stat, 25 ± 0.5°C). Error bars represent standard deviations of triplicate reactions (smaller than symbol if not visible). NR = no reaction observed.

Fig. 5. XRD patterns of (a) Ru/C and (b) Ru/Al_2O_3 collected after different *ex situ* pretreatments. Peaks assigned to Ru metal (○) and RuO_2 (*) are indicated.

Fig. 6. TPR profiles of (a) as-received Ru/C, (b) *ex situ* N_2 pretreated Ru/C, (c) *ex situ* H_2 pretreated Ru/C, (d) as-received Ru/Al_2O_3, (e) *ex situ* N_2 pretreated Ru/Al_2O_3, and (f) *ex situ* H_2 pretreated Ru/Al_2O_3. TCD signals are normalized with sample mass.

Fig. 7. (a) Comparison of Ru/C-catalyzed nitrite reaction kinetics with nitrate reaction at standard conditions (0.2 $g \cdot L^{-1}$ Ru/C, $[NO_3^-]_0$ or $[NO_2^-]_0$ = 1.6 mM). (b) TOF_0 of Ru/C-catalyzed nitrate and nitrite reduction as a function of initial concentration of the target oxyanion (0.2 $g \cdot L^{-1}$ Ru/C). (c) Measured timecourses for the simultaneous reduction of nitrate and nitrite added to a suspension containing Ru/C (0.2 $g \cdot L^{-1}$ catalyst, $[NO_3^-]_0 = [NO_2^-]_0$ = 1.6 mM). Other conditions include 1 atm H_2 continuous sparging, pH 5.0 maintained by automatic pH stat, and 25±0.5°C. Error bars in panels a-b represent standard deviations of triplicate reactions.

Fig. 8. Effect of initial (a) nitrate and (b) nitrite concentration on NH_4^+/N_2 product selectivity (yellow: NH_4^+; blue: N_2). Product selectivity is based on percent molar N concentration. Error bars represent standard deviations of triplicate reactions (smaller than symbol if not visible).

Fig. 9. Energy profile of the most thermodynamically favorable reaction pathways for aqueous nitrate and nitrite reduction on Ru_{18} clusters as calculated using PBE0 functional and LANL2DZ (Ru)/6-31+G(d,p)(N, H, O) basis sets.

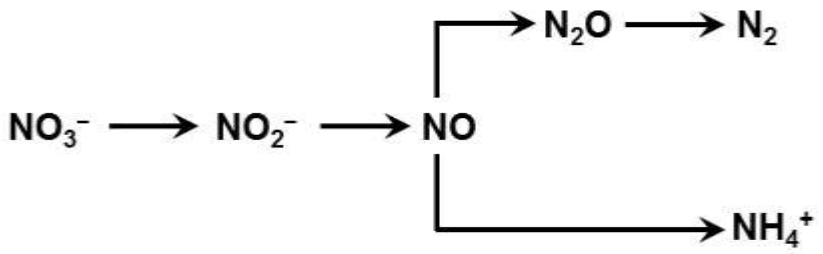

671

672 Scheme 1. Nitrate hydrogenation pathway on Pd-based bimetallic catalysts

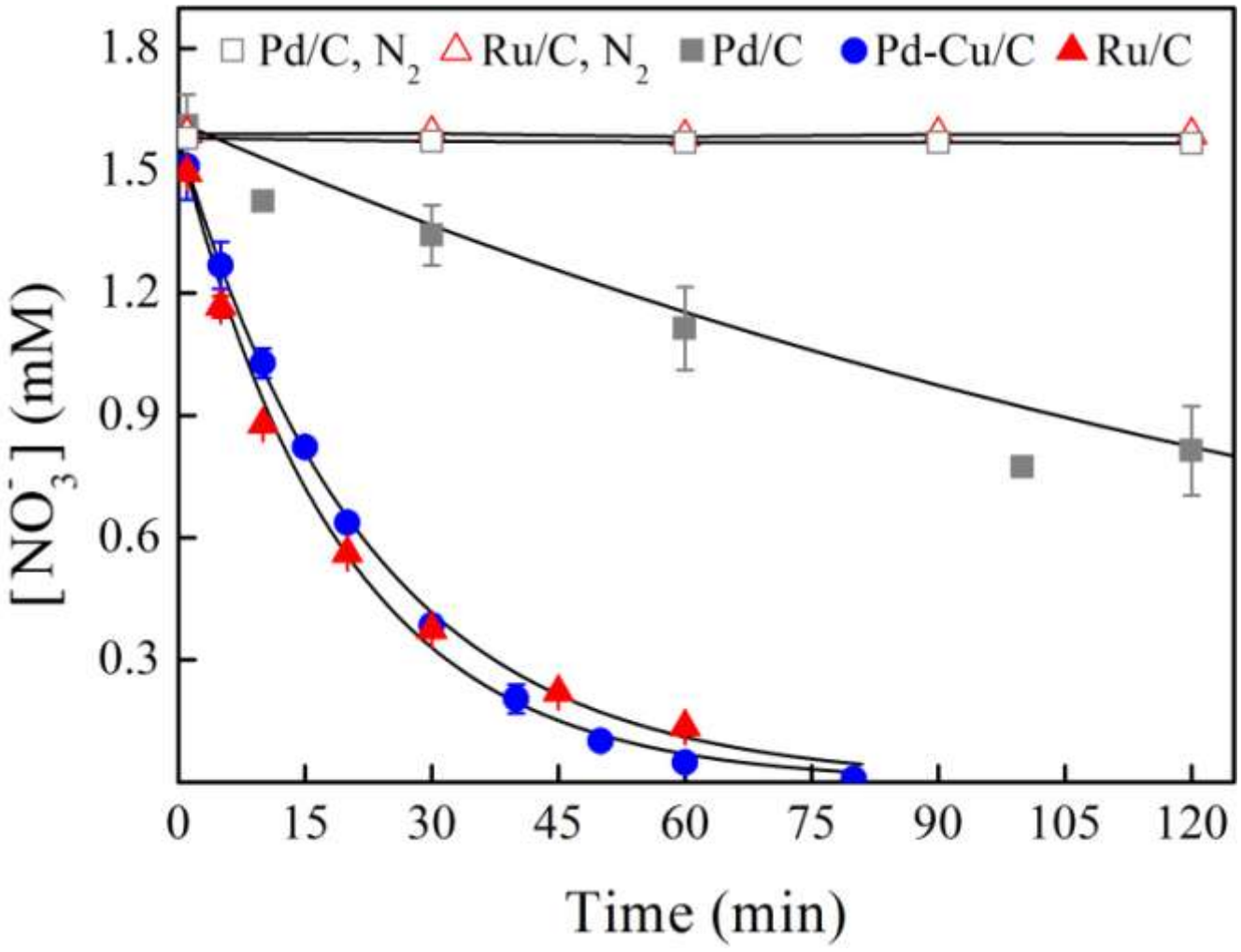

673

674 Fig. 1. Measured reaction timecourses for nitrate reduction and first-order model fits on 5 wt% Ru/C, 5
675 wt% Pd/C, and 5 wt% Pd-1 wt% Cu/C in the semi-batch reactor system (0.2 $g \cdot L^{-1}$ catalyst, $[NO_3^-]_0$ = 1.6
676 mM, 1 atm H_2 continuous sparging except in control experiments where 1 atm N_2 continuous sparging
677 was used, pH 5.0 maintained by pH stat, 25 ± 0.5°C). Error bars represent standard deviations of
678 triplicate reactions.

679 Table 1. Properties of catalysts used for nitrate activity test

Catalyst	BET surface area ($m^2 \cdot g^{-1}$)	Total pore volume[a] ($cm^3 \cdot g^{-1}$)	Average pore diameter[b] (nm)	Metal loading (wt%)	Metal dispersion (%)	Active surface (%)	Chemisorption particle size (nm)	TEM particle size (nm)	TOF_0 (min^{-1})[c]
Ru/C	859.7	0.74	3.46	5.38[d]	38	32	3.5	2.2±0.8	2.1±0.2
Ru/Al_2O_3	93.1	0.36	15.34	5[e]	15	9	8.8	8.1±3.0	2.4±0.5
Pd/C	856.9	0.72	3.35	6.24[d]	17	19	6.5	4.1±2.2	0.42±0.07
Pd/Al_2O_3	98.4	0.24	9.69	5.85[d]	16	15	6.9	4.2±1.1	NR[f]

680 [a]Adsorption total pore volume at P/P_0 = 0.97. [b]Calculated from total pore volume and BET surface area. [c]Calculated based on active surface. [d]Measured by
681 ICP-OES analysis. [e]Nominal value provided by supplier. [f]No reaction observed.
682

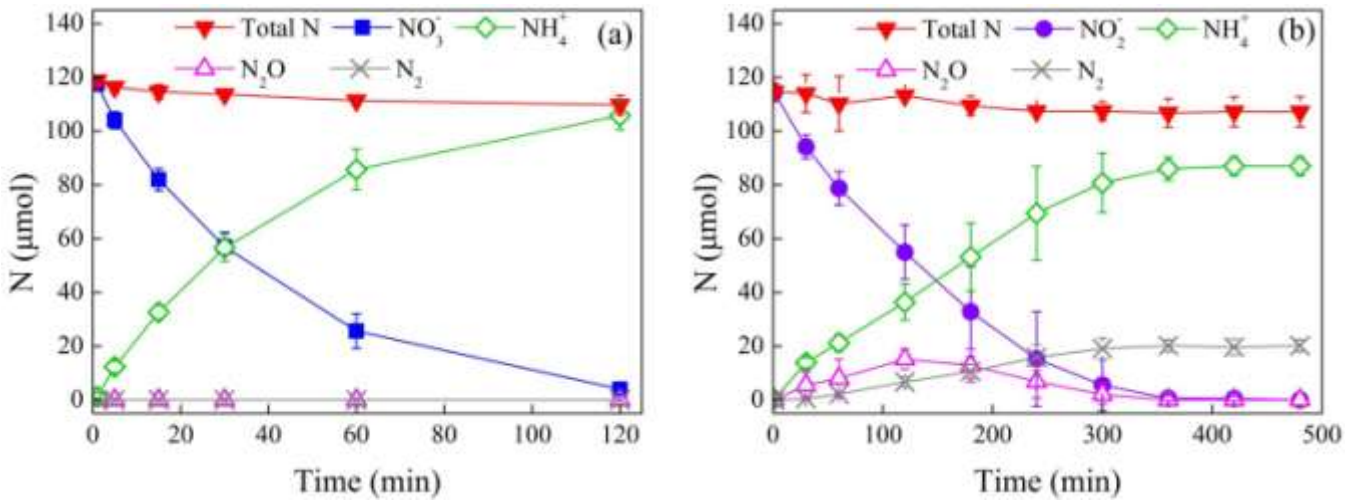

683

684 Fig. 2. Timecourses showing aqueous and gaseous intermediates and products during Ru/C-catalyzed
685 reduction of ^{15}N-labeled (a) nitrate and (b) nitrite monitored in closed-bottle batch systems (0.2 $g \cdot L^{-1}$
686 catalyst, $[^{15}NO_3^-]_0$ or $[^{15}NO_2^-]_0$ = 1.6 mM , initially 1 atm H_2, pH 5.5 buffered by 40 mM MES, 21 ±
687 1°C). Error bars represent standard deviations of triplicate reactions (smaller than symbol if not visible).

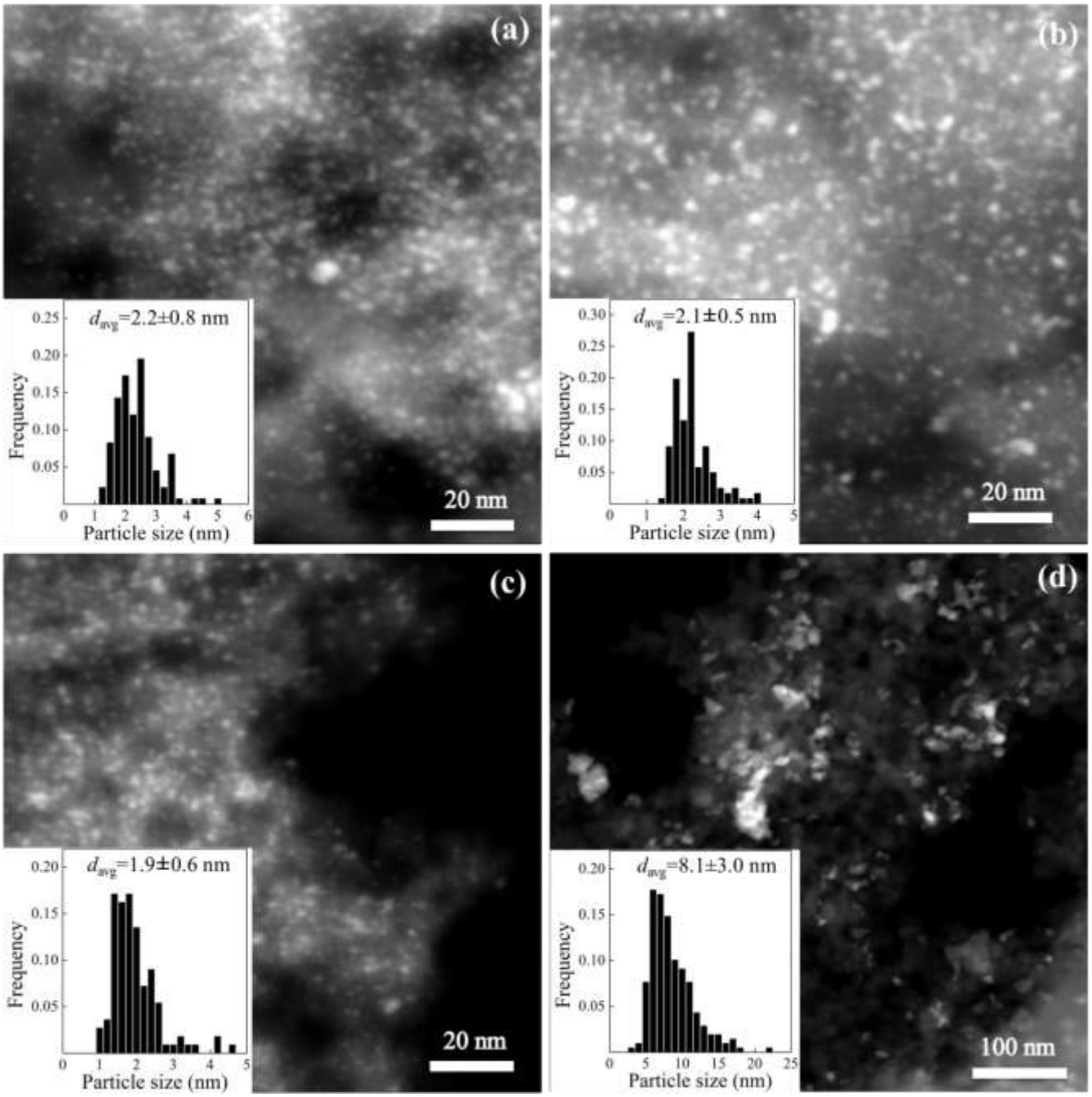

688

689 Fig. 3. HAADF-STEM images of (a) *ex situ* H_2 pretreated Ru/C, (b) Ru/C after re-use experiment, (c)
690 as-received Ru/C and (d) *ex situ* H_2 pretreated Ru/Al_2O_3. The insets show Ru particle size distributions.

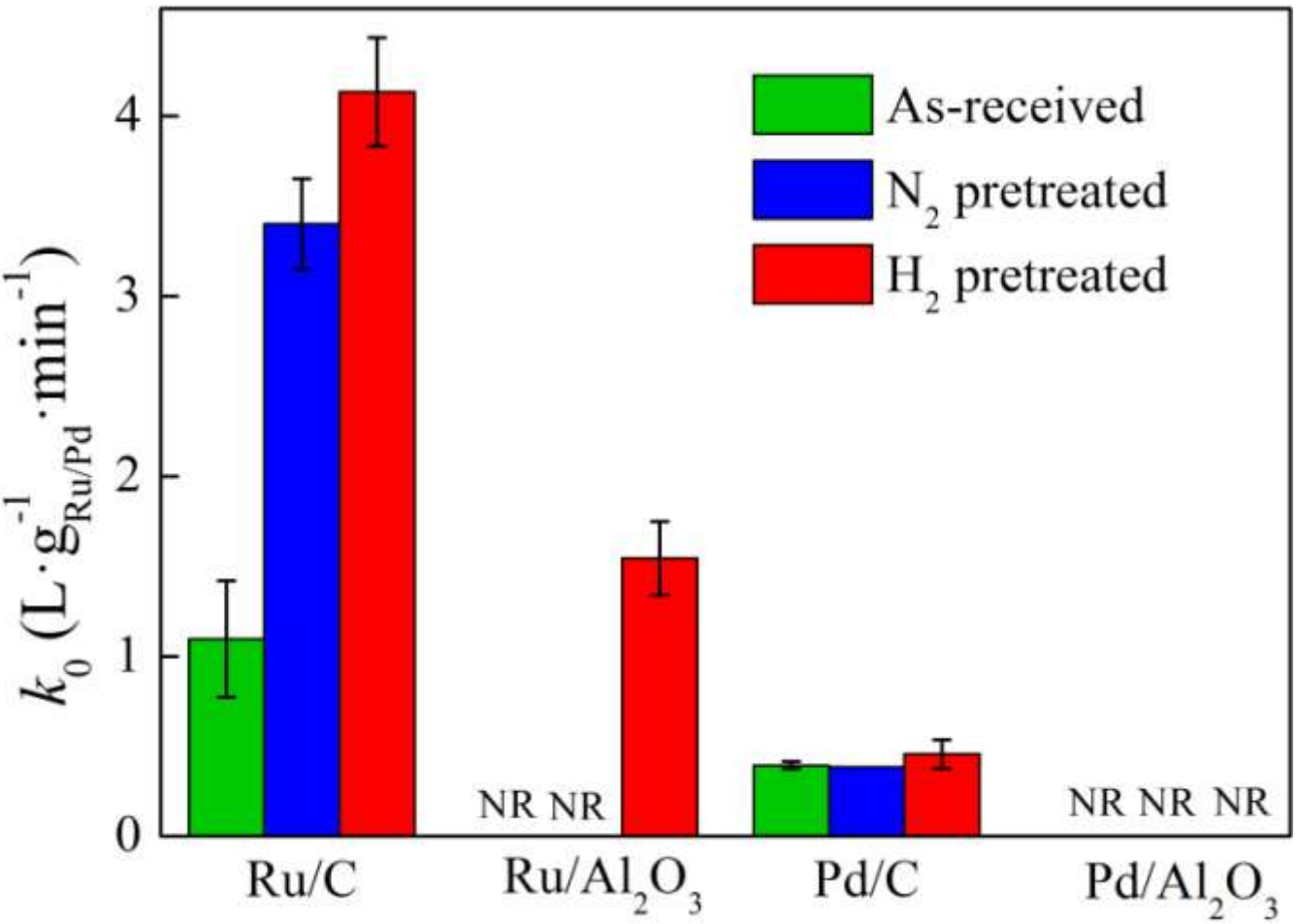

691
692 Fig. 4. Influence of catalyst pretreatments (as-received catalyst or *ex situ* pretreated in flowing H_2 or N_2
693 at 350 °C for 2 h) on reactivity with aqueous nitrate (0.2 $g \cdot L^{-1}$ catalyst with nominal 5 wt% Ru or Pd,
694 $[NO_3^-]_0$ = 1.6 mM, 1 atm H_2 continuous sparging, pH 5.0 maintained by automatic pH stat, 25 ± 0.5°C).
695 Error bars represent standard deviations of triplicate measurements (smaller than symbol if not visible).
696 NR = no reaction observed.

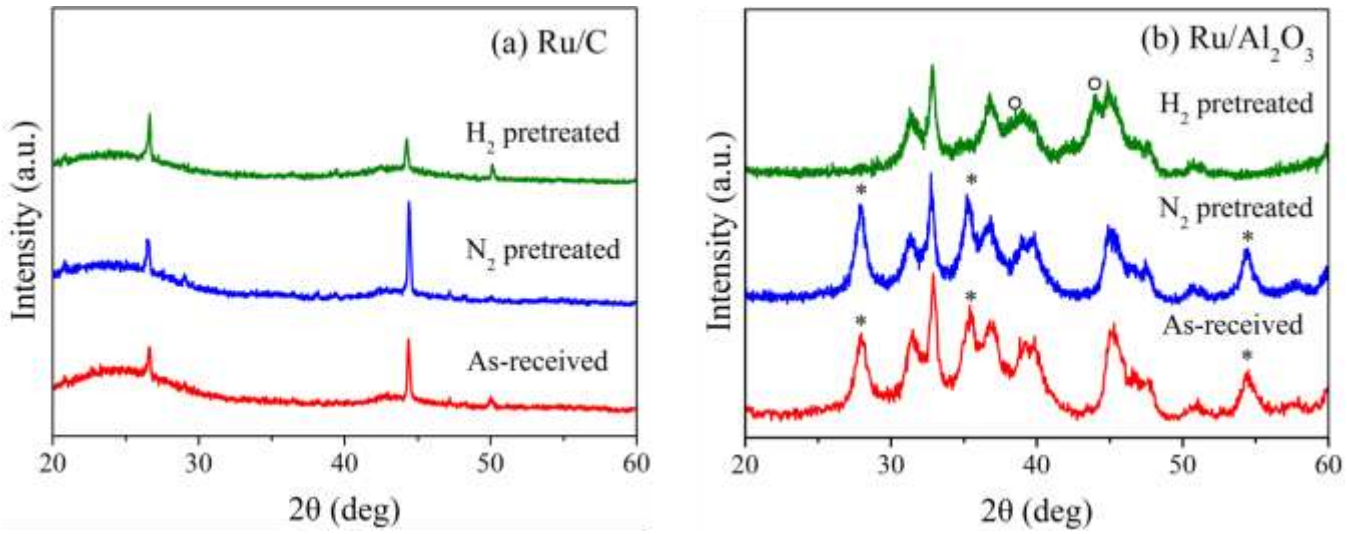

Fig. 5. XRD patterns of (a) Ru/C and (b) Ru/Al_2O_3 collected after different *ex situ* pretreatments. Peaks assigned to Ru metal (○) and RuO_2 (*) are indicated.

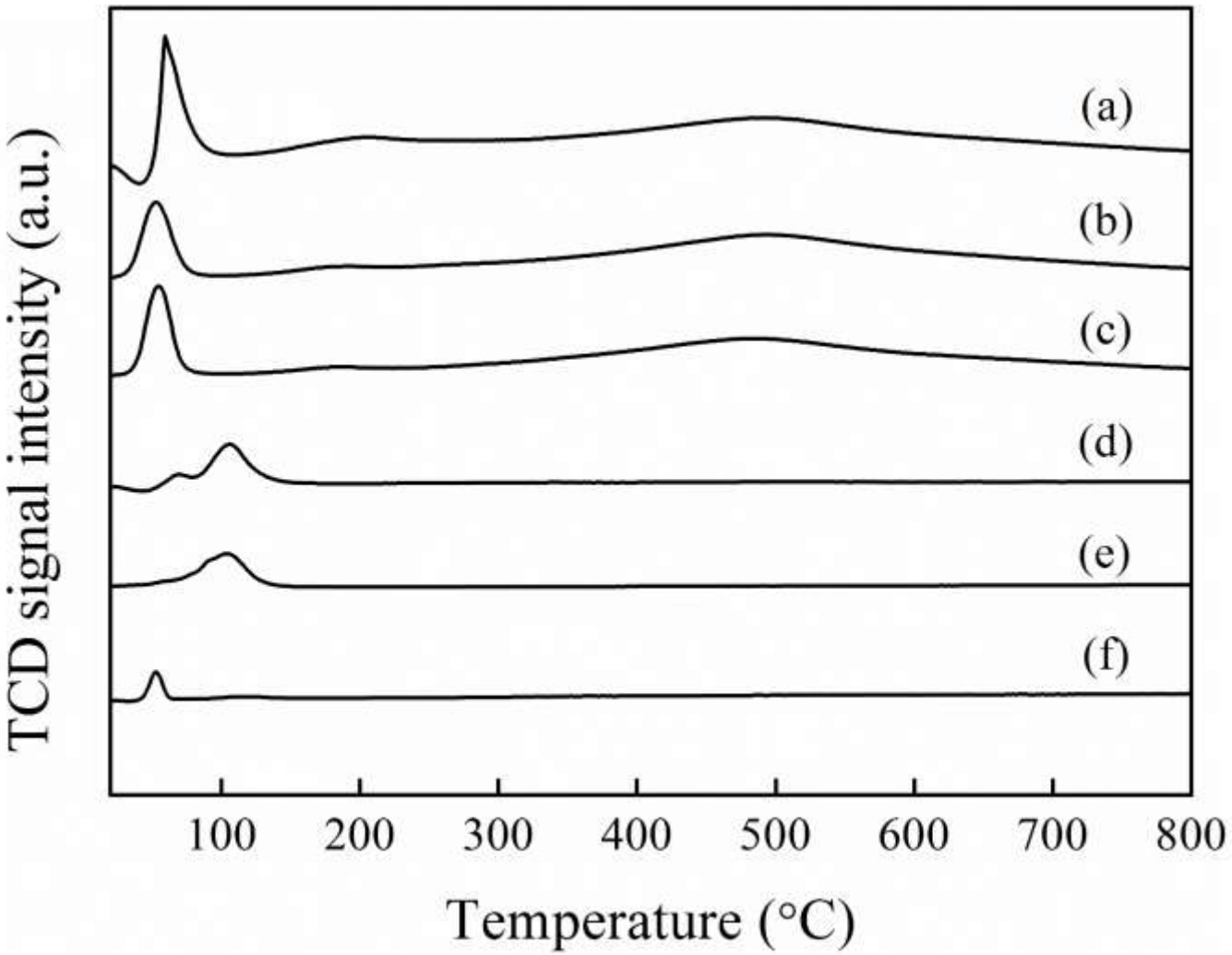

Fig. 6. TPR profiles of (a) as-received Ru/C, (b) *ex situ* N_2 pretreated Ru/C, (c) *ex situ* H_2 pretreated Ru/C, (d) as-received Ru/Al_2O_3, (e) *ex situ* N_2 pretreated Ru/Al_2O_3, and (f) *ex situ* H_2 pretreated Ru/Al_2O_3. TCD signals are normalized with sample mass.

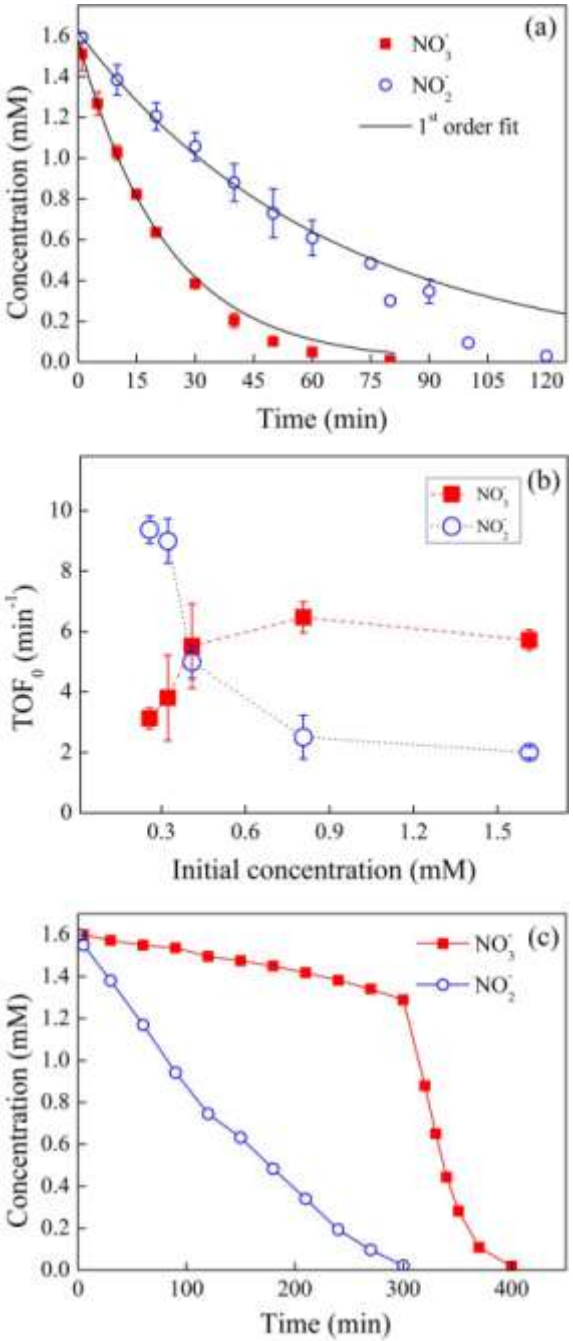

Fig. 7. (a) Comparison of Ru/C-catalyzed nitrite reaction kinetics with nitrate reaction at standard conditions (0.2 g·L^{-1} Ru/C, $[NO_3^-]_0$ or $[NO_2^-]_0$ = 1.6 mM). (b) TOF_0 of Ru/C-catalyzed nitrate and nitrite reduction as a function of initial concentration of the target oxyanion (0.2 g·L^{-1} Ru/C). (c) Measured timecourses for the simultaneous reduction of nitrate and nitrite added to a suspension containing Ru/C (0.2 g·L^{-1} catalyst, $[NO_3^-]_0 = [NO_2^-]_0$ = 1.6 mM). Other conditions include 1 atm H_2 continuous sparging, pH 5.0 maintained by automatic pH stat, and 25±0.5°C. Error bars in panels a-b represent standard deviations of triplicate measurements.

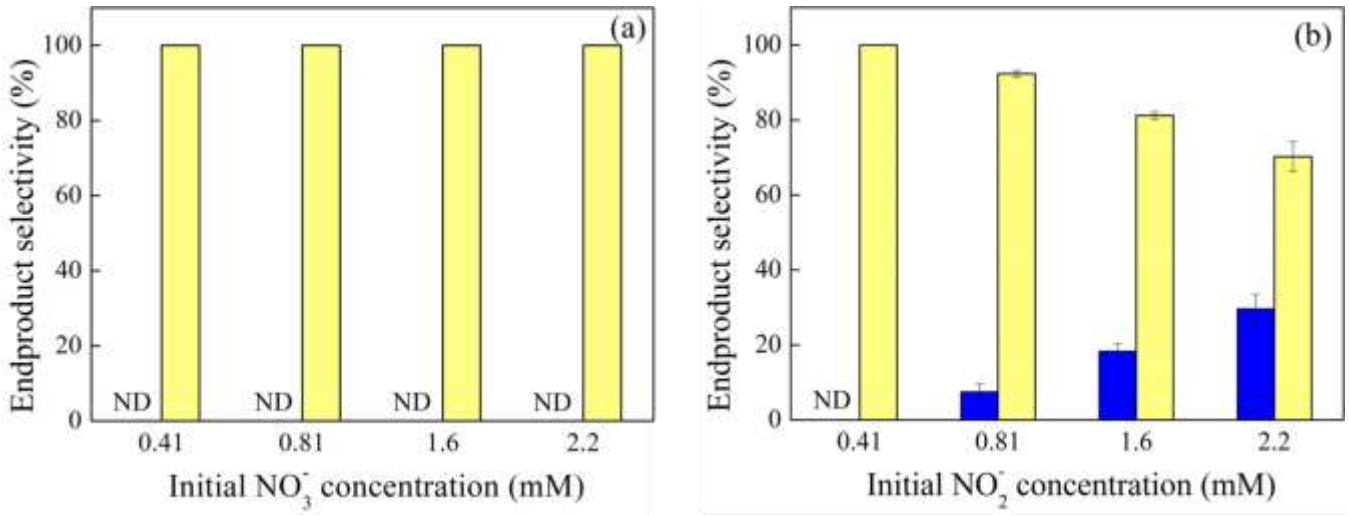

712

713 Fig. 8. Effect of initial (a) nitrate and (b) nitrite concentration on NH_4^+/N_2 product selectivity (yellow:
714 NH_4^+; blue: N_2). Product selectivity is based on percent molar N concentration. Error bars represent
715 standard deviations of triplicate measurements (smaller than symbol if not visible).

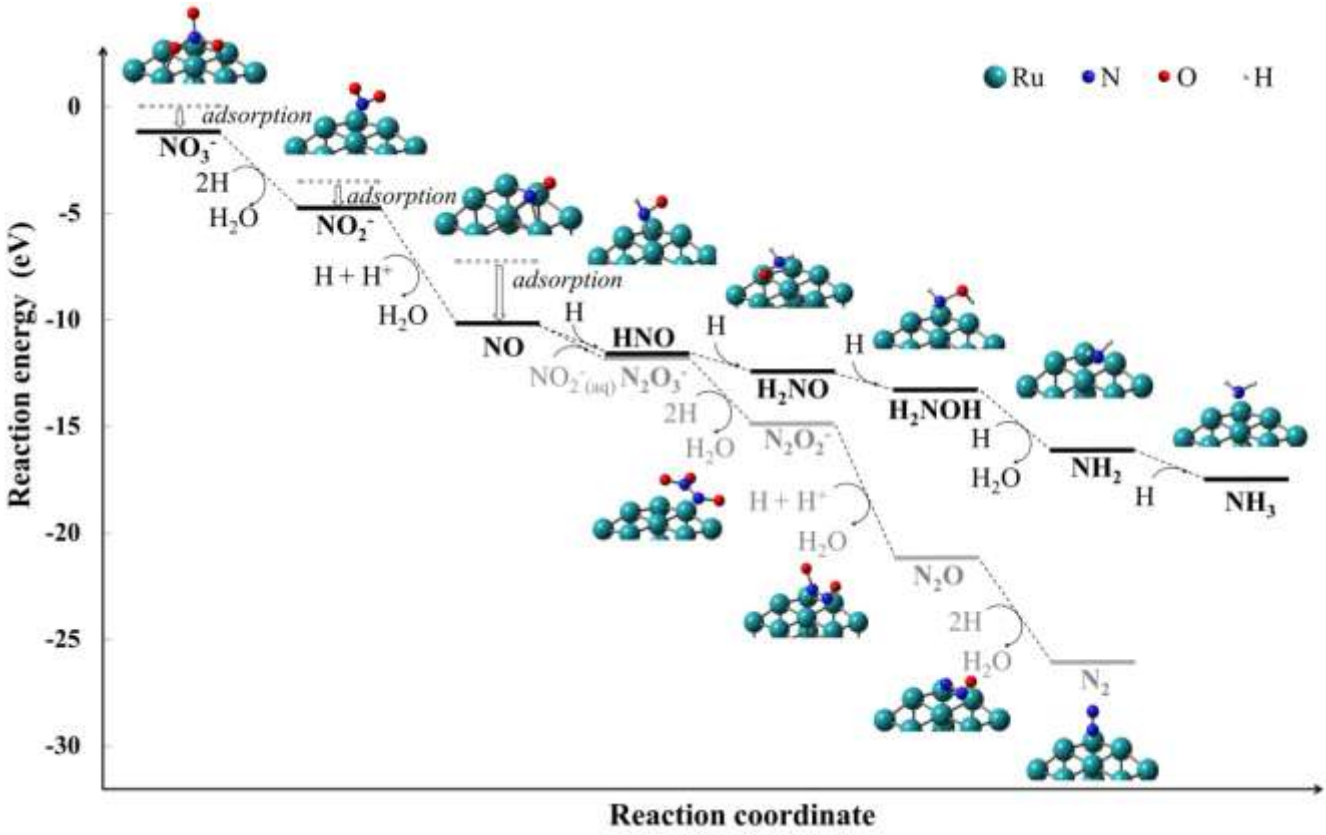

716

717 Fig. 9. Energy profile of the most thermodynamically favorable reaction pathways for aqueous nitrate
718 and nitrite reduction on Ru_{18} clusters as calculated using PBE0 functional and LANL2DZ
719 (Ru)/6-31+G(d,p)(N, H, O) basis sets.

720

721

722

723